Photocatalytic activity of a hydrothermally synthesized γ-Fe₂O₃@Au/MoS₂ heterostructure for organic dye degradation under green light

Pradeep Kumar [a], Utkarsh Kumar [a], Yu-Ching Huang [b], Po-Yo Tsai [a], Chia-Hao Liu [c], Chiu-Hsien Wu [a,c], Wen-Min Huang [a], Kuen-Lin Chen [a,c,*]

[a] *Department of Physics, National Chung Hsing University, Taichung 402, Taiwan*
[b] *Department of Materials Engineering, Ming Chi University of Technology, Taiwan*
[c] *Institute of Nanoscience, National Chung Hsing University, Taichung 402, Taiwan*

ARTICLE INFO

ABSTRACT

This article reports on a hydrothermally synthesized γ-Fe₂O₃@Au/MoS₂ heterostructure with excellent photocatalytic properties for the degradation of Methyl blue dye under green light at room temperature (300 K). The bandgap of the heterostructure was estimated from the Tauc plot and found as 0.91 eV (indirect) and 2.23 eV (direct). The optical and electrical activity of the heterostructure was revealed by the Raman spectra. The photocatalytic properties of γ-Fe₂O₃@Au/MoS₂ heterostructures were investigated by degrading Methyl Blue (MB) dye under green light (8 W) at various catalysis concentrations and pH values. Within 4 h, 98 % efficiency was achieved using a low amount of 0.01 gm catalyst with 1 ml H₂O₂ at a pH of 12. The pseudo-first-order reaction rate constant (K_{app}) revealed that no reaction occurred between MB and catalyst. Density functional techniques (DFT/B3LYP) with the LANL2MB basis set were used to calculate the energies, geometric structure, and vibrational numbers of MoS₂ and γ-Fe₂O₃@Au. DFT was used to extract the basic vibrational wavenumbers, intensities, and the shifting of energy levels for each step in the photodegradation reaction. A good agreement was found between the experimental and theoretical results.

1. Introduction

To improve living standards, various fields, such as medicine, agricultural, and industry are being developed. With 130 million newborns worldwide each year, obtaining clean water will be a significant challenge in the future. During the development process, a large number of perilous pollutants were arbitrarily discharged into the water in order to induce ecological contamination.[1] Toxic organic pollutants from domestic use and industrial activity are primarily responsible for the environmental problem. Harmful substances in industrial wastewater include engineered pigments and other natural pollutants. Every year, more than 1,000,000 business pigments(~7 × 10⁵ tons) are produced for use in industries like paper, material, restorative, printing, food, and pharmaceutical.[2] 8–20 % of unutilized dyes have been discharged directly into the water.[1] It causes cancer in humans and harms the environment. To obtain clean water, various techniques have been utilized to remove pigments from water.[2] At atmospheric pressure and temperature, photocatalytic degradation for water purification has

piqued the interest of researchers because it has the potential to convert hazardous dyes and organic contaminants in an aqueous solution into harmless CO₂, H₂O, or inorganic anions.[3] Photocatalyst has used Fenton oxidation, photocatalytic oxidation, photo-Fenton oxidation, and other advanced oxidation processes (AOPs)[4], to produce radicals such as superoxide radical (O_2^-),[5] hydroxyl radical (·OH), singlet oxygen ($^1O_2$) and reactive oxygen species (ROS).[6] Radicals were found to be responsible for the degradation of carbonic pollution in water.[7] Photo-Fenton and Fenton reaction occurs in photocatalysis due to magnetic compound, which is responsible for increasing the number of radicals.[8] On the other hand, plasmonic and semiconductor-based heterojunction can facilitate fast charge separation.[9] Because of surface plasmonic behavior, Au nanoparticles enhanced the rate of photo-Fenton reaction. The modification of metal nanoparticles (Ag, Au, Pt) can increase the activity in the visible region.[10]
.

In this study, a new heterostructure nanomaterial i.e. γ-Fe₂O₃@Au/MoS₂ was synthesized using the hydrothermal method. Various

advanced techniques were used for characterization including Fourier transform infrared spectroscopy (FTIR), Raman spectroscopy, UV–visible spectroscopy, X-ray diffraction (XRD), transmission electron microscopy (TEM), field emission scanning electron microscopy (FE-SEM), energy-dispersive X-ray spectroscopy (EDX), X-ray photoelectron spectroscopy (XPS), and dynamic light scattering (DLS). The photocatalyst was used in the presence of green light to degrade the methyle blue (MB) dye from water. The theoretical study was used to validate MB dye degradation based on changes in the HOMO-LUMO bandgap and molecular vibrations.

2. Computational analysis

The density functional theory (DFT)[11] was used to calculate the theoretical parameters of MoS_2/γ-Fe_2O_3@Au core–shell according to Becke's three parameters and the Lee-Yand Parr[12–14] functional (B3LYP) with LAND2MB basis set. Gaussian 09 package was used to calculate all the theoretical calculations.[15,77].

3. Results and discussion

The synthesis method and advanced instrumentation information are described in the Supporting information section **(SIS) 1**. TEM was used to examine the combination of MoS_2 nanoflakes and γ-Fe_2O_3@Au core–shell as shown in Fig. 1. The γ-Fe_2O_3@Au core–shell nanoparticles were submerged or soaked inside the MoS_2 nanoflakes as illustrated in Fig. 1(a-d). Au and γ-Fe_2O_3 have (111) crystal faces with d-spacing 0.26 nm and 0.53 nm respectively as illustrated in Fig. 1 **(d)**.[16] The particle size of γ-Fe_2O_3@Au/MoS_2 was calculated by using ImageJ software.[17] The thickness of MoS_2 nanoflakes around the core–shell increased the size of γ-Fe_2O_3@Au core–shell in the heterostructure. MoS_2 nanoflakes were found to be surrounding the γ-Fe_2O_3@Au core–shell **(Fig. 2 b).** As a result, the nanoarchitecture was named nanoflakes γ- Fe_2O_3@Au/MoS_2. The surface morphology of the synthesized compound has been analyzed by using FE-SEM and described in Fig. 2. The nanoflakes of the synthesized compound were visible in Fig. 2 **(a-b)** at the scales of 1 μm and 200 nm. The core–shell was completely covered with MoS_2 nanoflakes as shown in Fig. 2. Nonetheless, EDX mapping was used to investigate the presence of all possible elements, as shown in Fig. 2 **(c).** This showed that the synthesized compound has very high purity and no additional elements were found as illustrated in Fig. 2 **(d-h)**.

XRD spectra of γ-Fe_2O_3@Au/MoS_2 were examined in detail and compared to JCPDS data as illustrated in Fig. 3. The sample's less sharp and broader diffraction peaks indicate relatively poor crystallinity of γ-Fe_2O_3@Au on the MoS_2 support.[18,19] The presence of broader peaks at 35.5°, 44.36°, and 77.76° corresponding to (006), (009), and (001), respectively, confirms the presence of the rhombohedral and hexagonal crystal structures in MoS_2 nanoflakes. The peaks at 33.28°, 35.74°, 39.4°, 43.82°, 54.23°, and 38.23°, 44.69°, 77.76° were indicated by their Miller indices (104), (110), (006), (113) and (200), (220), (311) and (111), (200), (311) were identified as γ-Fe_2O_3 and Au respectively. γ-Fe_2O_3 was covered by Au, therefore, iron oxide's peaks were very poor. The **SIS-4** Table 1 describes the explanation of each XRD peak and its comparison with the JCPDS data in detail.

In Fig. 2(d-h) the coexistence of molybdenum (Mo), sulfur (S), gold (Au), iron (Fe), and oxygen (O) was revealed by the EDX spectrum of γ-Fe_2O_3@Au/MoS_2, which was also confirmed by the XPS study (Fig. 4). The binding energies of iron oxide were calculated to be 706.7 eV, 709.6 eV, 710.8 eV, and 712.1 eV.[20,21] The binding energies of Fe $2p_{3/2}$, O 1 s, and Au $4f_{7/2}$ were 708 eV (Fig. 4 **e)**, 529.8 eV (Fig. 4 **d)**, and 84 eV (Fig. 4 **b)**. The sulfur 2 s region is strongly overlapping with the Mo 3d state. The binding energies of Mo 3d (229.09 eV, 232.07 eV) and S 2p (162.085 eV) are depicted in **Fig. (4c)**. Mo 3d XPS spectrum revealed excited states $3d_{5/2}$ and $3d_{3/2}$ at 229.09 eV and 232.07 eV respectively, whereas S $2p_{1/2}$ and O 1 $s_{1/2}$ have only excited states at 162.085 eV and 530 eV respectively. In stoichiometric MoO_3, 435.9 eV binding energy corresponded to Mo^{+6}.[22] In **Fig. (4b)**, the peaks at 37.25 eV, and 63.69 eV represent the Mo 4p and Mo 4 s. **SIS-4** Table 2 mentions new oxidization and shifting XPS peaks with a good comparison. Peak shifting due to core–shell oxidation of outer sulfur (S—O) of MoS_2 flakes. [23] This could be due to the defects in the MoS_2 outer layers. As a result, a combination of S vacancies and metallic Mo clusters was formed.[23] According to the XPS result, the oxidation processes of Mo and S occurred. This was also one of the reasons why the radical quantity in the photocatalysis chemical reaction was increased.

4. Optical property analysis

4.1. Molecular vibration based on FT-IR

The FTIR spectra of γ-Fe_2O_3@Au/MoS_2 as well as the theoretically

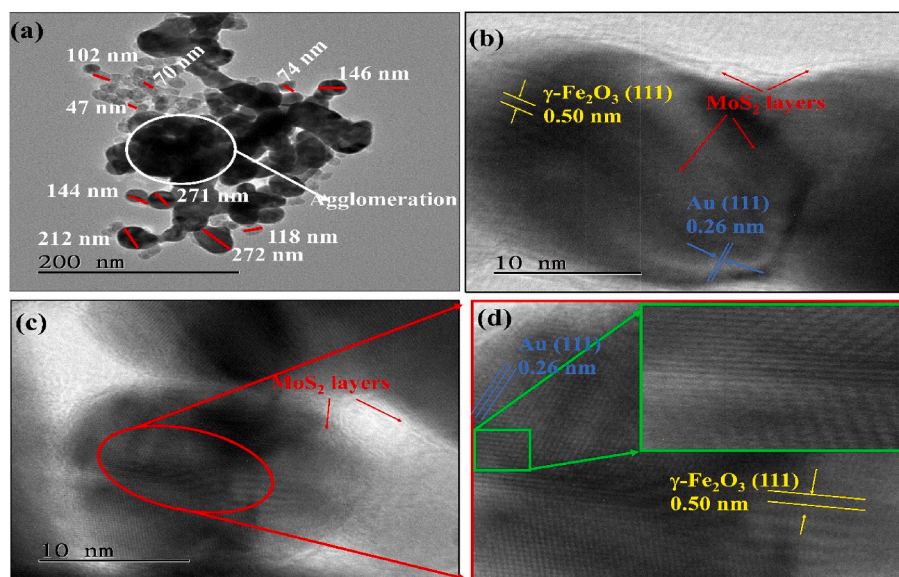**Fig. 1.** **(a-d)** High-magnification cross-sectional TEM image of MoS_2 nanoflakes agglomerated with γ-Fe_2O_3 clearly shows the layered structure of MoS_2 nanosheets and core–shell of γ-Fe_2O_3.
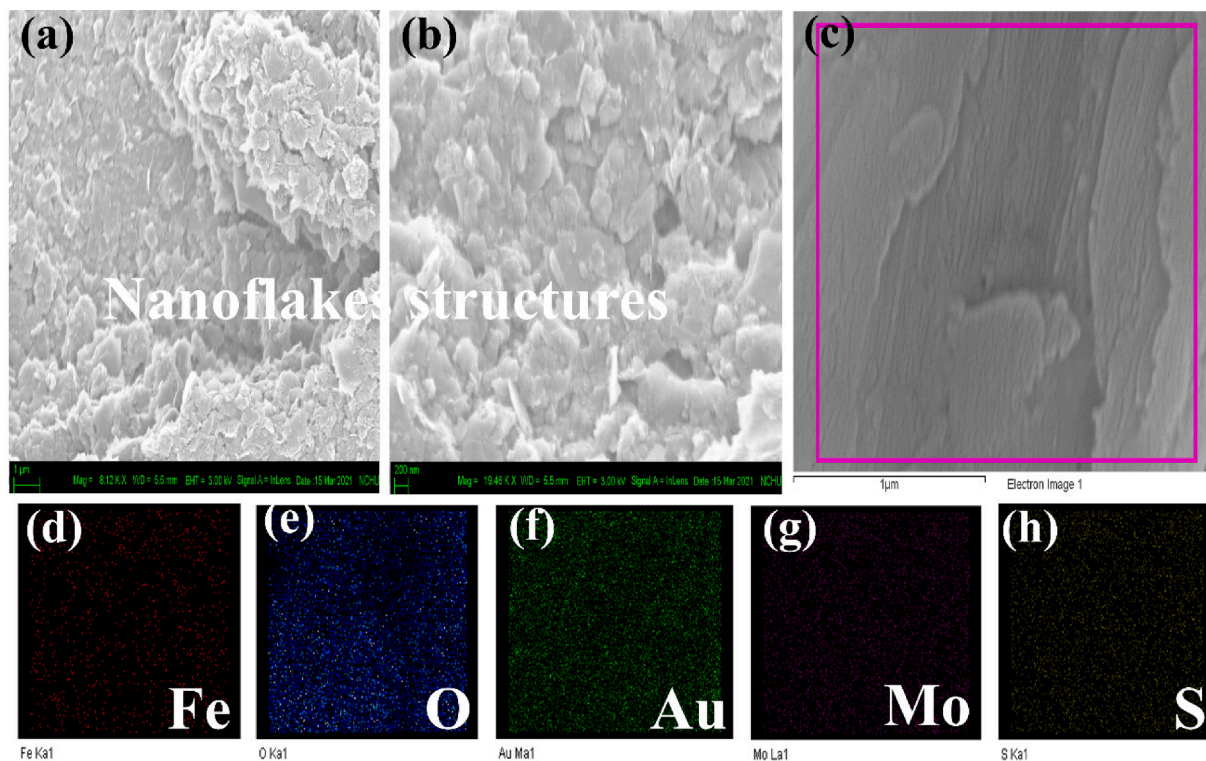
Fig. 2. (a-c) The morphological and (d-i) EDX mapping analysis of γ-Fe2O3@Au/MoS2-based products by FE-SEM.
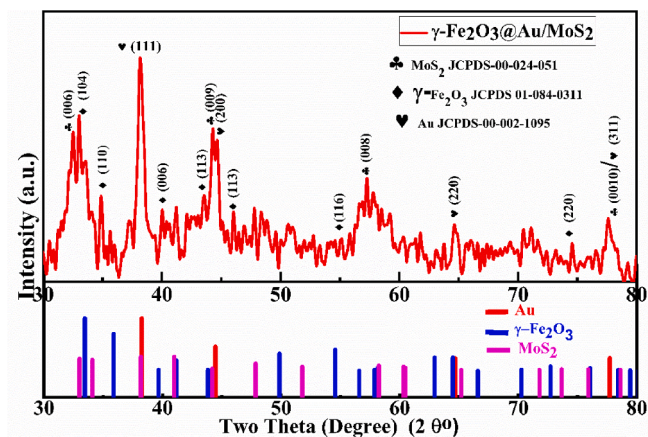

Fig. 3. XRD spectra of MoS$_2$ nanoflakes agglomerated with γ-Fe$_2$O$_3$@Au.

Table 1
Experimental FTIR and computed vibrational wavenumber (cm^{-1}) along with the assignment of Fe$_2$O$_3$@Au/MoS$_2$.

Wavenumber in cm^{-1}		Assignment
Experimental	Theoretical	
415	415	S-Mo stretching
421, 425, 450	423	S-Au stretching
465	467	In-plane MoS$_2$ streching
551	554	Fe = O out of plane blending
674, 690	683	O = Fe = O stretching
1223	1219	Fe = O stretch of Au

calculated spectrum using DFT/B3LYP/LAN2MB are illustrated in Fig. 5 and agree well with the experimental spectra. The total energy distribution (TED), showed the relative contributions of the redundant internal coordinates to each normal vibrational mode of the molecule and thus allowed numerically defining the nature of each mode. Peaks Below 700 cm^{-1} belong to the Mo-O deformation mode, which could be caused by the sulfidation vibration.[24] The different experimental and theoretical vibrational peaks have been shown in Table 1. The comparison in transmission between γ-Fe$_2$O$_3$, γ-Fe$_2$O$_3$@Au, and γ-Fe$_2$O$_3$@Au /MoS$_2$ was explained in the **SIS-4 Table-2.**

4.2. UV–Visible absorbance spectra

In the previous study, it has been found, that MoS$_2$ has different optical UV–vis spectra, due to the 1 T,[25] 2H[26], and 3R modes.[27] The Brillouin Zone K point in 2D MoS$_2$ has been assigned as 454 nm and 400 nm.[28] These bands originated due to interband transition between the occupied d_z^2 orbit and unoccupied d_{xy} $d_{x^2-y^2}$ and $d_{xy,yz}$ orbitals. [29]. In the UV–vis spectra, the Au peak at 560 nm[30,31] (Fig. 6a) has good absorbance. Au peaks disappeared in the heterostructure, and two excitons (smooth) peaks at 545 nm and 719 nm (Fig. 6b) were found. The region colored blue, yellow, and red colors represents the γ-Fe$_2$O$_3$, Au, and MoS$_2$ optical absorbance spectra Fig. 6 **(a-b)**. The absorbance shifting in the UV–vis spectra of γ-Fe$_2$O$_3$@Au/MoS$_2$ has been assigned by γ-Fe$_2$O$_3$@Au. Using UV–visible spectra, the direct/indirect bandgaps of γ-Fe$_2$O$_3$@Au and γ-Fe$_2$O$_3$@Au/MoS$_2$ were calculated and found to be 3.07 eV/0.94 eV and 2.23 eV/0.91 eV respectively, as illustrated in Fig. 6 **(c-d)**. Nonetheless, the direct/indirect bandgap of heterostructure was reduced when compared to γ-Fe$_2$O$_3$@Au. The heterostructure has a lower bandgap than visible light. As a result, the excited electron can easily move from the valance band to the conduction band. Dielectric constant decreases with an increase in the bandgap for nanoparticles. [32] This compound has dielectric confinement and can absorb photons quickly without being disturbed.[33,34] As a result, it may lead to potential optoelectronic and nanoelectronic applications.[35–37] Absorbance shifting demonstrated quantum confinement, dielectric confinement, and edge effect.[38].
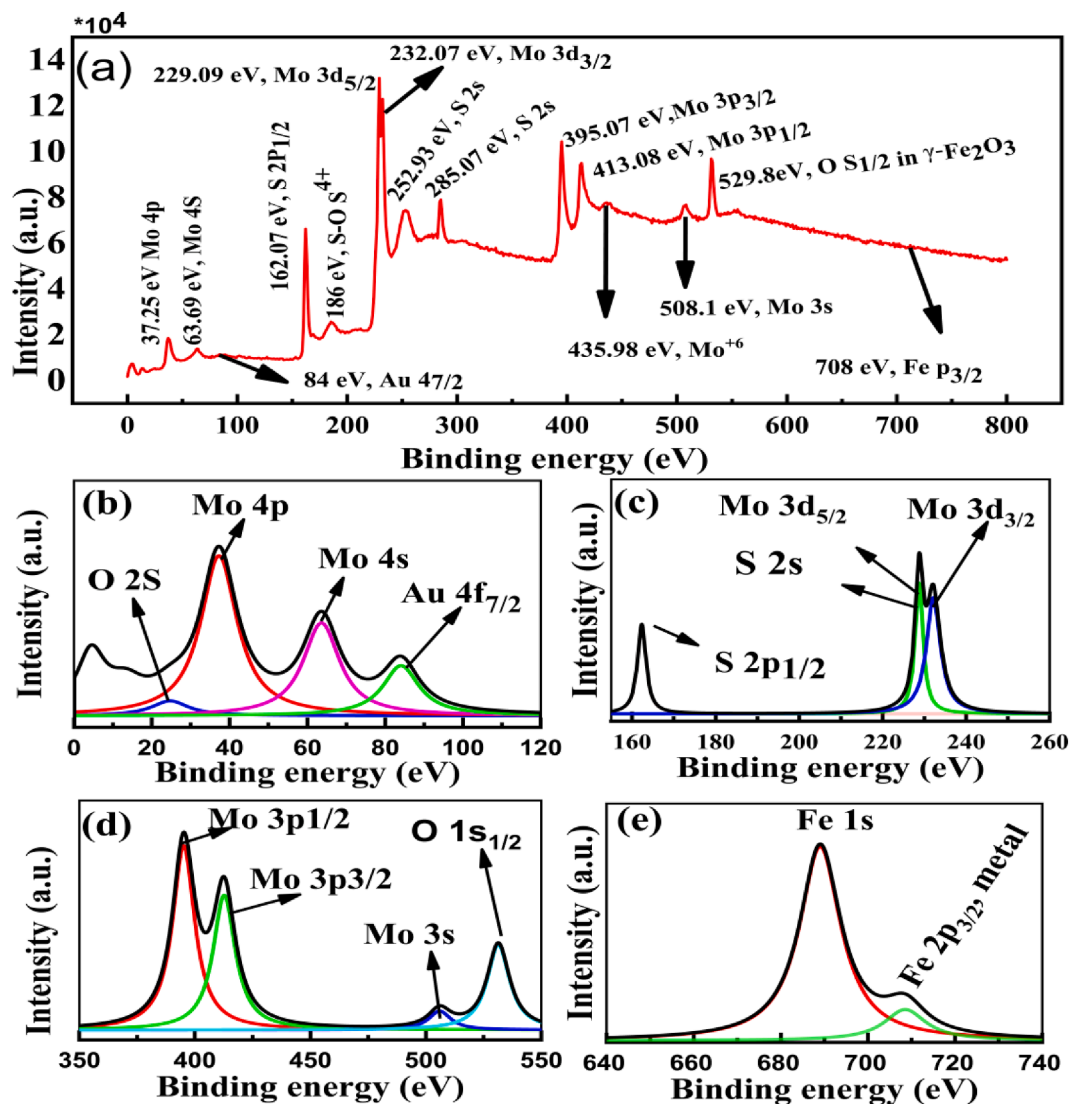
Fig. 4. (a-e) X-ray photoelectron spectroscopy (XPS) Mo, S, Au, and Fe in the different excited states.

Table 2
A comparative study of photocatalytic properties for degradation of MB Dyes with those reported in the literature.

Composition Name	Source	Degradation efficiency %	Reference
Fe_2O_3-TiO_2/SF	–	94.2 %	[56]
Ag/AgCl	443 nm laser	90.8	[57]
n-SnO_2/p-CFO	Sun light	87	[58]
TiO_2/AC-(L)	UV	99.43	[59]
MoS_2/graphene	10 w white LED	97.8	[60]
MoS_2/SA-Fe^{3+}	Infrared laser	98	[61]
γ-Fe_2O_3/$SrTiO_3$	Visible light	84.91	[62]
Co-α-Fe_2O_3	Visible light	91.8	[63]
γ-Fe_2O_3@Au/MoS_2	Green LED	98	This work

5. Anomalous lattice vibrations analysis

The absolute Raman intensities were calculated using the intensity theory of Raman scattering and the Raman activities (S_i) acquired with the Gaussian 09 software,

$$I_i = \frac{f(v_0 - v_i)^4 S_i}{v_i[1 - \exp\left(-\frac{hcv_i}{KT}\right)]} \tag{1}$$
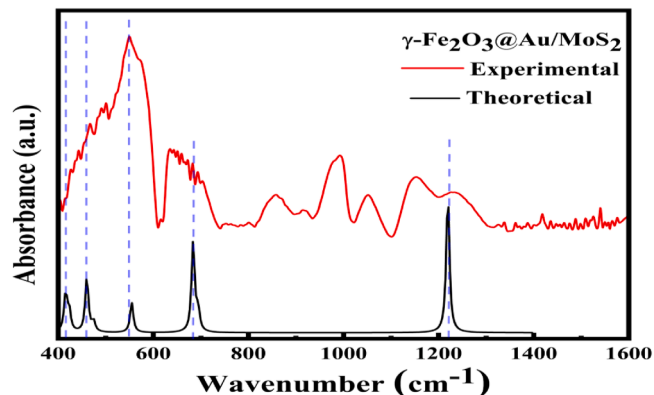
Fig. 5. Theoretical and experimental FTIR spectra of Fe_2O_3@Au/MoS_2.

where v_0 and v_i are the laser exciting wave number and vibrational wavenumber of ith mode in cm^{-1}, and Raman scattering activity of normal mode was represented by S_i with f as a normalizing factor. The k, h, c, and T have been denoted as Boltzmann, Plank constants, speed of light, and temperature, respectively. Fig. 7 depicts the experimental and
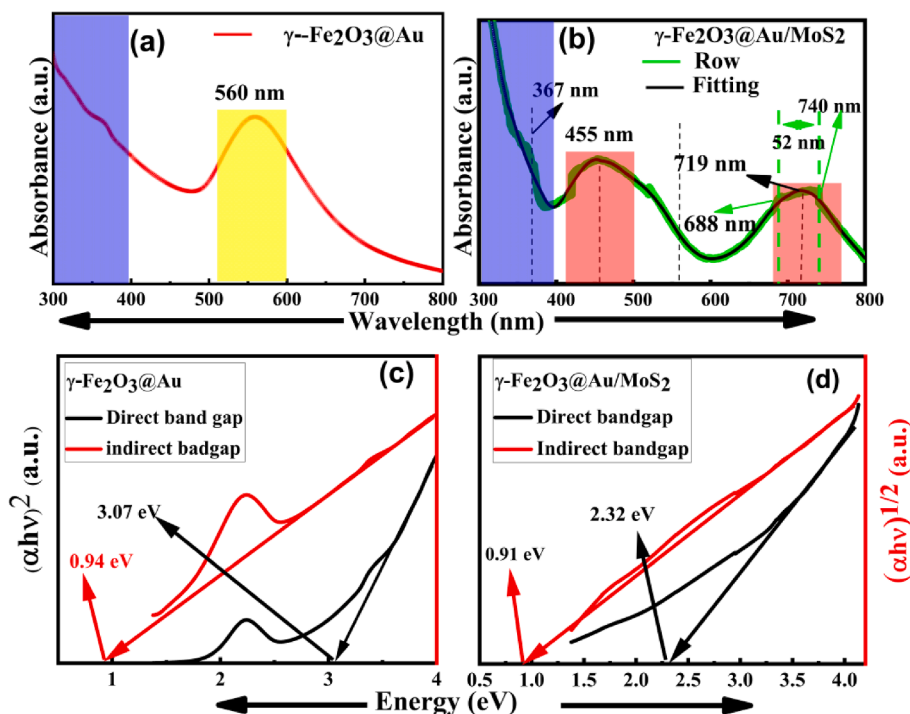
Fig. 6. (a,b) UV light absorbance spectra of γ-F$_2$O$_3$@Au and γ-F$_2$O$_3$@Au/MoS$_2$. (c-d) direct/ indirect band-gap of γ-F$_2$O$_3$@Au and γ-F$_2$O$_3$@Au /MoS$_2$.
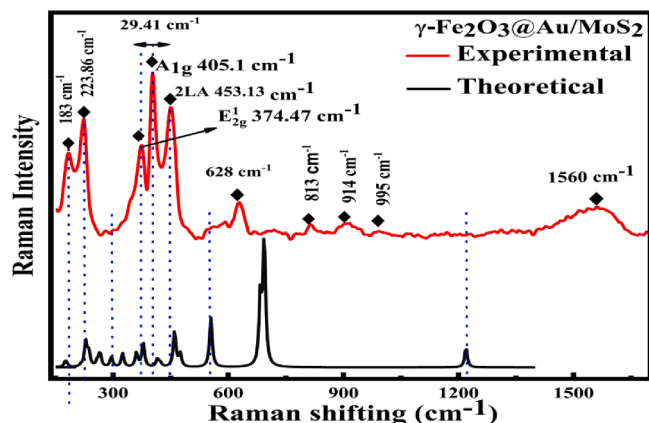
Fig. 7. The Raman shifting at room temperature of MoS$_2$ nanoflakes agglomerated with γ-Fe$_2$O$_3$@Au characterized by Raman spectra.

theoretical Raman investigation of γ-Fe$_2$O$_3$@Au/MoS$_2$. The comparison of Raman peaks between γ-Fe$_2$O$_3$, γ-Fe$_2$O$_3$@Au, and γ-Fe$_2$O$_3$@Au/MoS$_2$ has been explained in **SIS-3,** additional standard orientation and Distance matrix (angstroms). The shifting of Raman peaks could be seen in Fig. 7. MoS$_2$ exhibits atomic vibration at 192 cm^{-1}, ZA (M); 278 cm^{-1}, E$_{1g}$ (Γ); 332.8 cm^{-1}, E$_{2u}$ (M); 377 cm^{-1}, $E_{2g}^1(M)$; 449 cm^{-1}, A$_{2u}$ (Γ); 656 cm^{-1}, $A_{1g}^1 - LA$(M)^h; 820 cm^{-1}, and 2*A$_{1g}$ (Γ)0.991 cm^{-1}.[47,48] [39] γ-Fe$_2$O$_3$ has Raman active modes at 355 cm^{-1} (E$_{1g}$), 381 cm^{-1} (T$_{2g}$), 510 cm^{-1} (T$_{2g}$) and the peaks around 600 cm^{-1} to 805 cm^{-1} also represent the Raman vibration for γ-Fe$_2$O$_3$.[40,41] The lower energy of Raman laser has been used which is comparable to the bandgap of the MoS$_2$ and responsible for the excitation.[42,43].

The most strongly observed Raman active phonon modes for MoS$_2$ were 374 cm^{-1} (E), 405 cm^{-1} (A$_{1g}$), 453 cm^{-1} (2LA), while iron-oxide peaks were 223.86 cm^{-1}, 183 cm^{-1}, 628 cm^{-1}. Au Raman peaks around 1560 cm^{-1} have been identified.[30] The unusual behavior of the longitudinal acoustic mode (LA) occurs near the midpoint of the Brillouin zone.[44] The enhancement in 2LA mode has occurred due to coupling resonance.[45] The similarity between the experimental data and theoretical data for Raman's peaks is shown in Fig. 7. A$_{1g}$ phonons were stronger than the E_{2g}^1 phonons because of excited d_z^2 state. Therefore, the intensity of A$_{1g}$ has been optimized more intense compared to the E_{2g}^1. The atomic vibration between the inner and outer layers determoines the structure of any compound. Therefore, the structural change was caused by the highly active A$_{1g}$ mode. This indicates the presence of anomalous lattice vibrations,[43] anisotropic properties, higher energy excitation transition, thermal effect,[46] optical absorbance, and Vander-Waals force. In the previously reported data,[43] the difference between E_{2g}^1 and A$_{1g}$ modes has been found to be 3 cm^{-1} for a single layer of MoS$_2$.[43] As a result, the energy difference between E_{2g}^1 and A$_{1g}$ vibration modes of Mo-S was ~ 29 cm^{-1} corresponding to 5–8 nanosheets.[47] The broader peak of E_{2g}^1 indicates that a simple harmonic motion (SHO) in a plane covered a large displacement, which increased the effective restoring force acting on the atoms due to the long-range Coulbombic interlayers Van der Waals interaction.[43] The increase and decrease in the broadening of E_{2g}^1 and A_g^1 peaks belong to anomalous behaviors. Therefore, it implies that this compound has a flexible behavior.[43] The coupling of phonon in an interlayer plane belongs to small sensitivity to thickness of the E_{2g}^1 mode. LSPR property was observed due to enhancement in the intensity of the A_g^1 and anomalous behaviors of E_{2g}^1. [48] As a result, 2LA vibration was found with good intensity. The application and synthesis methods of some MoS$_2$ compositions have been organised in **SIS-3.**

From **SIS-3** it was found that broadening in the peaks of Raman spectra and lower bandgap of the material make them suitable for photocatalysis. According to the above characterizations like TEM, Raman, and XPS, it can say that γ-Fe$_2$O$_3$@Au /MoS$_2$ was promising for catalysis application. This is the first paper to describe a multi-layered core–shell γ-Fe$_2$O$_3$@Au/MoS$_2$ with multiple photocatalysis and long-term durability.

6. Photocatalyst measurement

The kinetic model[49] is useful to describe the pathways of the catalytic reaction. The catalytic reaction involves several reaction conditions, including the concentration of H_2O_2, the amount of catalyst, medium, and concentration of MB. 2 ml (0.0156 M) MB was mixed in 200 ml DI. A small amount of 0.01 g γ-Fe_2O_3@Au/MoS_2 was added to the solution. Before irradiation, the solution was mechanically stirred in dark for 60 min to ensure the formation of an adsorption–desorption equilibrium.[50] The above solution was then mixed with 35 %, 1 ml of H_2O_2 (pH 1.8), and the mixture was irradiated under a green LED light. The compound's photocatalytic efficiencies were evaluated using the degradation of MB at room temperature and an 8-watt green LED light. These steps were repeated for different concentrations of (0.02 gm and 0.03 gm) γ-Fe_2O_3@Au /MoS_2 and pH (4.48, 7, 10 & 12). Otherwise, the conditions remained the same as the first trial. The solution was irradiated continuously for three days after adsorption–desorption equilibrium at 0.01 gm γ-Fe_2O_3@Au /MoS_2 (pH 4.48) to learn about the behavior of catalyst for degradation of MB. The catalysis properties of γ-Fe_2O_3@Au/MoS_2 were performed at 7 pH and without H_2O_2 as shown in **SIS-5** Fig. 4. After adding γ-Fe_2O_3@Au/MoS_2 catalyst, the reaction occurred, resulting in dye color removal. The degradation efficiency, ratio, and degradation rate of MB were calculated using Eqns. 2, [2,51,52] 3, 4,[53–55] and 5. The 1.5 μl solution and 2.5 μl DI were placed in a cuvette to determine the degradation effect over time. The kinetic properties were measured with a UV–Visible spectrometer at room temperature (300 K).

$$(\eta) Efficiency\,\% = \left(\frac{A_o - A_t}{A_o}\right) * 100\,\%$$

$$Ratio = \frac{A_t}{A_o}$$

$$\log(A_o/A_t) = K_{app} * t$$

$$Degradation\ Rate = \frac{Change\ in\ absorbance\ magnitude}{Change\ in\ time}$$

where A_o is the initial absorbance magnitude of 2 ml MB in 200 ml DI, A_t is finial absorbance magnitude of MB, K_{app} are pseudo-first-order reaction rate constant (min^{-1}) and t was the time in minute, respectively.

7. Photocatalysis characterization

The UV–vis. absorbance spectra of MB degradation were shown in Fig. 8(a & b). The absorbance magnitude of the pure MB absorbance curve decreased with time and has two major peaks 612 nm and 661 nm.
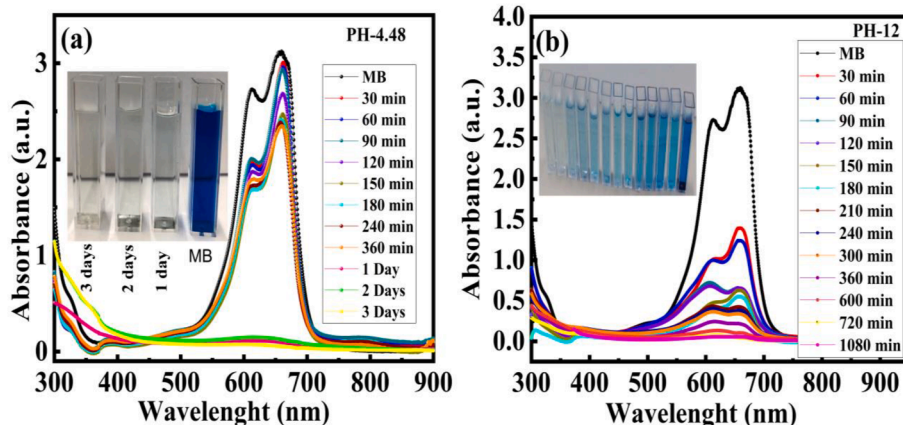
Fig. 9 depicts the kinetic behavior of catalysis at different concentrations and pH values. Without H_2O_2, the MB degradation of catalysts was tested at 0.01 gm and 4.48 pH. In this condition, the degradation efficiency was reached at ∼ 20 % after 10 hrs as illustrated in **SIS-5** Fig. 5. The kinetic behavior of catalysts (0.01 gm & 4.48 pH) for both peaks was similar in the form of an exponential as shown in Fig. 9 (a & b). The degradation rate of the peak 661 nm was reached at 0.00156 from 0.0034 in dark, indicating that the solution was in adsorption–desorption equilibrium.[54] The degradation rate (0.155384) was increased within the next 30 min, which was 99 times faster than in dark. After adding H_2O_2, the kinetic properties of the MB degradation followed the pseudo-first-order reaction (Fig. 9b) and the pseudo-first-order reaction constant was 3.12×10^{-4} min^{-1}. As a result, no reaction occurred between MB and catalysis. Almost all dye color was removed after 24 hrs and the degradation efficiency was reached ∼ 98 % at 0.01 gm catalysts and 4.48 pH. Different conditions, such as different concentrations of catalysis and pH, were used to improve degradation efficiency/time.

As well as the concentration of catalysis was increased then the degradation rate and efficiency were increased. (Fig. 9c). Nonetheless, as shown in Fig. 9 (d), the pseudo-first-order reaction constant (min^{-1}) was also increased. The degradation rate, **pseudo**-first-order reaction constant, and efficiency were more effective at higher pH values as illustrated in Fig. 9 (e & f). At 12 pH, the degradation efficiency reached 93.5 % after 360 min. Nonetheless, in a few hours, all blue color disappeared and the efficiency reached 98 %. The degradation result at 7 pH and the recycling process have been discussed in **SIS-5**. This material has good stability for photocatalytic and can be used for the recycling process as illustrated in **SIS-5** Fig. 10. γ-Fe_2O_3@Au/MoS_2 showed slightly higher activity during the first-round test, and the degradation rate slightly declined after four test rounds.

8. Mechanism

The various pathways (Fig. 10) to degradation of MB were calculated by the simulation using Gaussian. MB's degradation with various pathways was made possible by the follow-up reactions 6–14 involved in the chemical reaction.[52,54,64,65] The chemical activity of γ-Fe_2O_3@Au /MoS_2 with MB in dark and light has been illustrated in Fig. 11. The mobility of the electrons increased as H_2O_2 was added,[66] resulting in more ions in the solution and faster degradation of MB under green light irradiation. The interaction of light and oxygen in presence of moisture produces oxidizing radicals and ROS.[67] Nonetheless, Au exhibits plasmonic behavior under green light and plays an important role in enhancing MB degradation. Au increased the number of holes-electrons pairs and promoted the breakdown of H_2O_2 into ·OH.

Fig. 8. Time-dependent UV–Visible absorbance spectra of degradation of MB for 0.01 gm catalyst at pH values of (a) 4.48 and (b) 12.
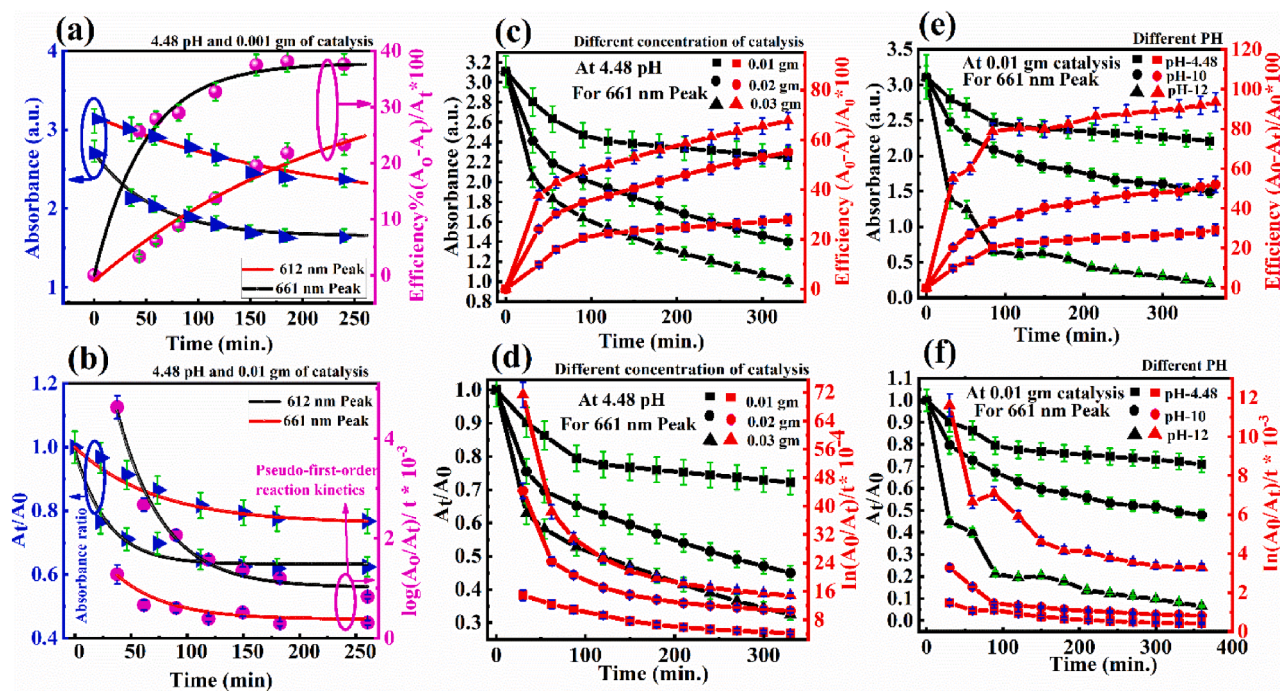
Fig. 9. Photocatalyst degradation of MB a, c, e absorbance, and degradation efficiency; b, d, f absorbance A_t/A_o ratio, and are pseudo-first-order reaction rate constant (min^{-1}) at different concentrations of catalysis and different pH with time.
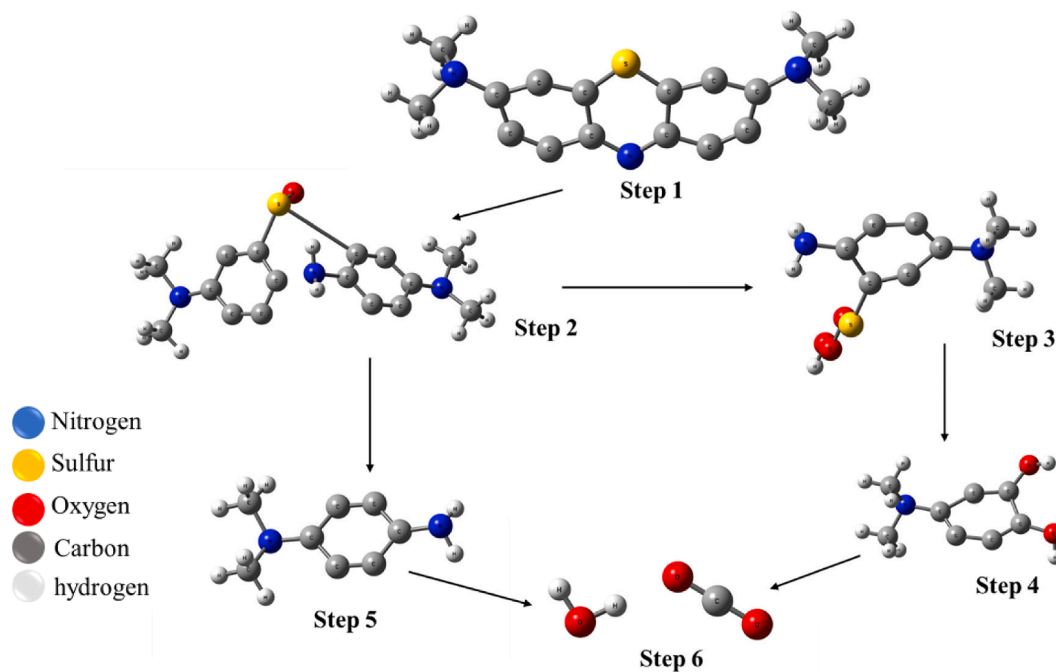

Fig. 10. The degradation pathways of methyl blue reacting with photocatalytic oxidant.
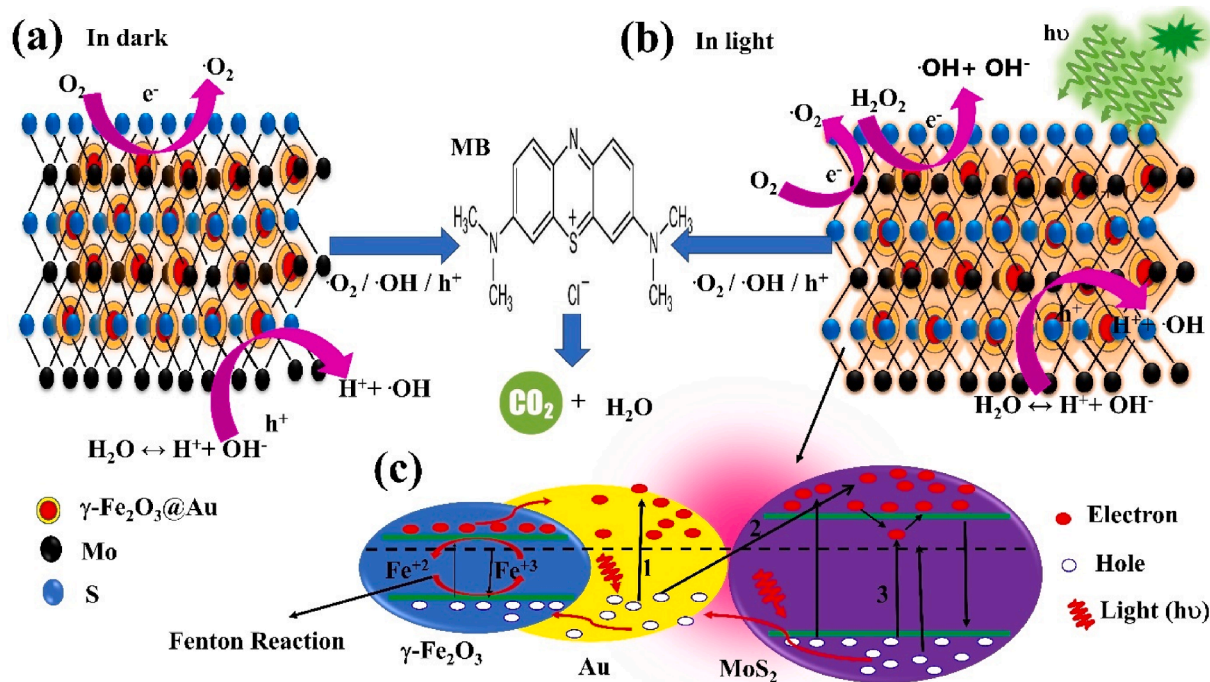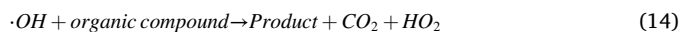
Fig. 11. Mechanism of degradation in dark and green light.

$$MoS_2 + h\upsilon \rightarrow MoS_2 + h^+ + e^- \qquad (6)$$

$$Au \rightarrow Au^+ + e^- \qquad (7)$$

$$Fe^{+2} \leftrightarrow Fe^{+3} + e^- \qquad (8)$$

$$O_2 + e^- \rightarrow O_2^- \qquad (9)$$

$$H_2O_2 + e^- \rightarrow \cdot OH + OH^- \qquad (10)$$

$$H_2O \leftrightarrow H^+ + OH^- \leftrightarrow \cdot OH + h^+ \qquad (11)$$

$$\cdot OH + H_2O_2 \rightarrow \cdot HO_2 + H_2O \qquad (12)$$

$$\cdot HO_2 \rightarrow O_2^- + H^+ \qquad (13)$$

$$\cdot OH + organic\ compound \rightarrow Product + CO_2 + HO_2 \qquad (14)$$
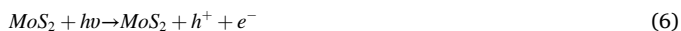
Small Schottky barriers were formed due to the contact of Au and MoS_2 at the equilibrium state,[68] then the mobility of charge carriers were stopped. Therefore, the degradation rate became extremely low. When the green light was turned on, then Au quickly released electrons, due to which the mobility of charge carriers in γ-Fe_2O_3[69,70] and MoS_2 was increased. As illustrated in Fig. 11 (c), various photocarrier with distinct routes (1, 2 & 3 routes) were active in the system. The process by which plasmon-induced "hot electrons" are generated and reach the outer surface is known as plasmon-induced electron transfer (PIET) (route 1).[71] These electrons were quickly absorbed by oxygen and increased the number of ROS. Another plasmon-induced interfacial charge transfer to the conduction band of MoS_2 via route 2. The number of electrons was generated as a result of surface plasmon decay and plasmon-induced interfacial charge-transfer transition (PICTT).[71] Enhanced light absorbance causes the formation of electron-hole pairs in MoS_2, which can be extracted using a light source (route 3). The electromagnetic field and localization's enhancement increased the absorbance of light surrounding MoS_2.[68] ROS have been identified as the potential substance for destroying original pollutants in wastewater. In comparison to oxygen molecules, superoxide radical (O_2^-)[72], hydroxyl radical ($\cdot OH$)[72], singlet oxygen ($^1O_2$) and ROS are highly
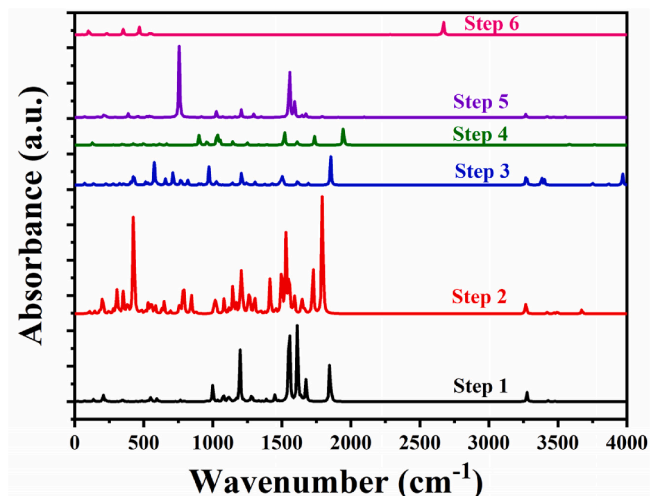
Fig. 12. Theoretical FTIR analysis of degradation process.

reactive molecules. In presence of H_2O_2, a large no. of ROS were produced in green light. Therefore, the degradation efficiency of MB was a more than 98 %.

The photodegradation mechanism and shifting of energy level were also verified by theoretical calculations. In this analysis, we analyzed the change in the vibrational spectrum of the molecules during each degradation process and found that the results were very similar to our experimental results.

From FTIR data, when the OH molecules interacted with MB, then oxygen and hydrogen get attached to the sulfur and the nitrogen respectively, resulting in the formation of no peak between 2200 and 2600 cm^{-1} **(step 6)**. The molecule dissociates from the center due to the difference in the energy levels, as shown in Fig. 12. The presence of benzothiazole in the solution is indicated by a strong peak ranging from 50 to 400 cm^{-1}. When methyl blue is dissolved in water, Cl is separated first. During the bombardment of the radical species, the N-CH$_3$ link is initially broken and the –CH$_3$ is oxidized into HCHO or HCOOH. As

Fig. 13. Shifting of energy levels during photodegradation. The red and green colors indicate negative and positive charges for the title molecules respectively.

shown in the FTIR spectrum of steps 3, 4, and 5 the C—S and C—N bonds on methylene blue's core heterocycle are easily disrupted by the free radical attack, yielding 2,5-diaminobenzenesulfonic acid and 4-amino-catechol. The formaldehyde and 2,5-diaminobenzenesulfonic acid are used to make benzothiazole. These intermediates are eventually oxidized to a single ring structure, producing CO_2 and H_2O.

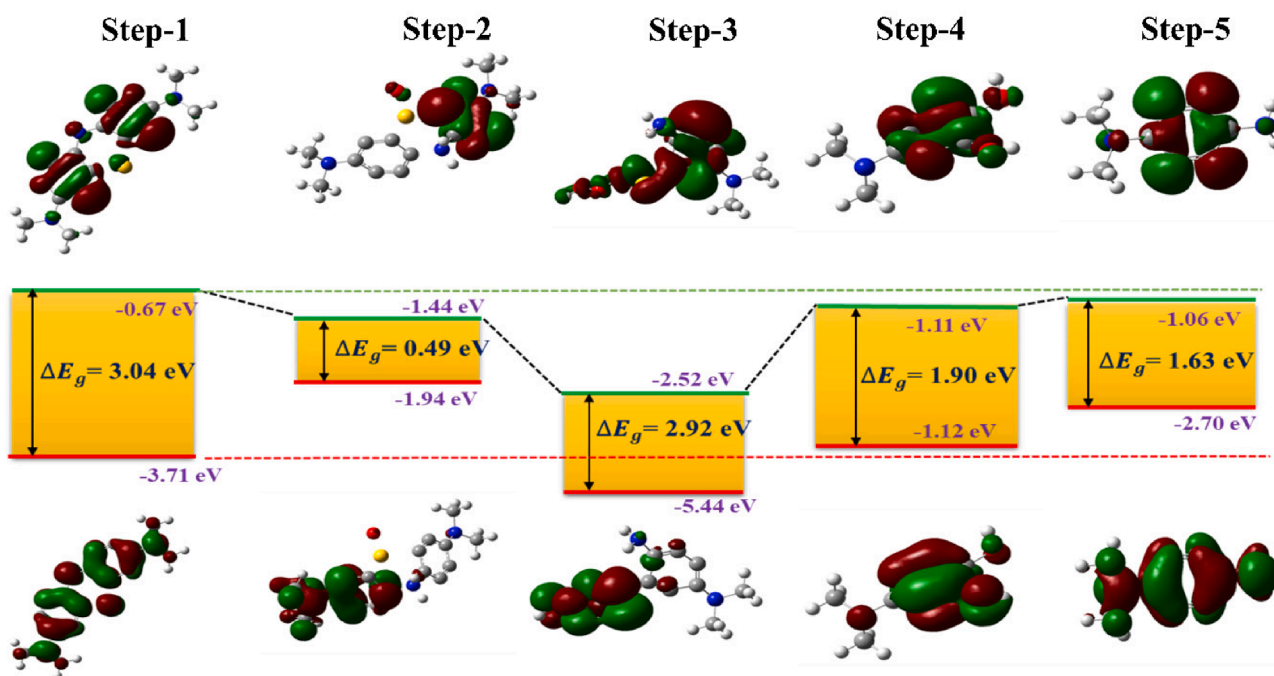The shifting of energy levels was analyzed by the HOMO (higher occupied molecular orbitals) and LUMO (lower unoccupied molecular orbitals) during each step and illustrated in Fig. 13. As it can be seen from Fig. 13, the energy gap of methyl blue is 3.04 eV based on the calculated HOMO (−3.71 eV) to LUMO (−0.67) molecular energy level. This study also demonstrates that when MoS_2 ions interact with the methyl blue, the energy gap was grammatically reduced to 0.49 eV. This change in energy was responsible for the degradation of methyl blue in some non-toxic materials. HOMO-LUMO energies were important in governing a wide range of chemical interactions. [73–76]. The optical energy gap significantly influenced the photocatalytic degradation effect of γ-Fe_2O_3@Au/MoS_2. The calculated HOMO-LUMO energy gap reveals that the main π conjugation and electron density of the γ-Fe_2O_3@Au increases by introducing electron-donating substituent MoS_2. As a result, the photodegradation rate of the degradation of MB was enhanced.

9. Conclusion.

In this study, the γ-Fe_2O_3@Au/MoS_2 heterostructure was successfully synthesized by the hydrothermal method and characterized. The presence of the new XPS peaks showed that this compound has a weak Van der Waals force and MoS_2 defects, which made it easy to remove electrons from the surface. The direct/indirect bandgap 2.32 eV/0.91 eV was calculated. The enhancement in the 2LA Raman vibration mode was a good indication of the coupling of the resonance condition to the electronics associated with the excitonic state. Plasmonic behaviors, weak Van der Waals force, semiconductor property, and presence of MoS_2 defects made it unique for photocatalysis to degradation. It has excellent catalyst properties for reducing the water pollution caused by dyes. At a low amount (0.001 g) of catalyst and (1 ml, 35 %) H_2O_2, the degradation efficiency was reached more than 98 %. The experimental

characterization results and degradation phenomena were verified by the theoretical results using density functional techniques (DFT/B3LYP). The changes in the HOMO-LUMO energy gap of each degradation step reveal that the main π conjugation and electron density of the γ-Fe_2O_3@Au increases by introducing electron-donating substituent MoS_2.

CRediT authorship contribution statement

Pradeep Kumar: Writing – review & editing, Writing – original draft, Visualization, Validation, Methodology, Investigation, Formal analysis, Data curation, Conceptualization. **Utkarsh Kumar:** Writing – review & editing, Software, Formal analysis. **Yu-Ching Huang:** Writing – review & editing, Supervision, Formal analysis. **Po-Yo Tsai:** Methodology. **Chia-Hao Liu:** Methodology. **Chiu-Hsien Wu:** Writing – review & editing, Supervision, Resources. **Wen-Min Huang:** Writing – review & editing, Supervision, Resources. **Kuen-Lin Chen:** Writing – review & editing, Visualization, Supervision, Resources, Project administration, Methodology, Investigation, Formal analysis, Data curation, Conceptualization.

Declaration of Competing Interest

The authors declare that they have no known competing financial interests or personal relationships that could have appeared to influence the work reported in this paper.

Data availability

Data will be made available on request.

Acknowledgments

Appendix A. Supplementary data

Supplementary data to this article can be found online at https://doi.org/10.1016/j.jphotochem.2022.114186.

References

[1] S. Singh, P. Chaudhary, R. Srivastava, R. Kant Tripathi, R. Kumar, B.C. Yadav, Improved growth of nano tin ferrites with their decoration on carbon foam for wastewater treatment, Environ. Nanotechnol. Monit. Manag. 16 (2021), 100546, https://doi.org/10.1016/j.enmm.2021.100546.

[2] A.M. El-Sawy, A.H. Gemeay, A.S. Helal, M.A. Salem, Catalytic degradation of methylene blue in aqueous solution by H2O2 and SiO2-NH2-Cu(II)@SiO2 nanoparticles as catalyst, J. Mol. Liq. 341 (2021), 117422, https://doi.org/10.1016/j.molliq.2021.117422.

[3] Z. Wang, F. Zhang, A. Ning, D. Lv, G. Jiang, A. Song, Nanosilver supported on inert nano-diamond as a direct plasmonic photocatalyst for degradation of methyl blue, J. Environ. Chem. Eng. 9 (1) (2021) 104912, https://doi.org/10.1016/j.jece.2020.104912.

[4] R. Dewil, D. Mantzavinos, I. Poulios, M.A. Rodrigo, New perspectives for Advanced Oxidation Processes, J. Environ. Manage. 195 (2017) 93–99, https://doi.org/10.1016/j.jenvman.2017.04.010.

[5] M. Hayyan, M.A. Hashim, I.M. AlNashef, Superoxide Ion: Generation and Chemical Implications, Chem. Rev. 116 (2016) 3029–3085, https://doi.org/10.1021/acs.chemrev.5b00407.

[6] K. Das, A. Roychoudhury, Reactive oxygen species (ROS) and response of antioxidants as ROS-scavengers during environmental stress in plants, Front. Environ. Sci. 2 (2014), https://doi.org/10.3389/fenvs.2014.00053.

[7] J.H. Baxendale, J.K. Thomas, The degradation of polymethacrylic acid by ultraviolet and X-irradiation, Trans. Faraday Soc. 54 (1958) 1515–1525, https://doi.org/10.1039/TF9585401515.

[8] Y. Liu, W. Jin, Y. Zhao, G. Zhang, W. Zhang, Enhanced catalytic degradation of methylene blue by α-Fe2O3/graphene oxide via heterogeneous photo-Fenton reactions, Appl. Catal. B Environ. 206 (2017) 642–652, https://doi.org/10.1016/j.apcatb.2017.01.075.

[9] KK. Paul, P.K. Giri, Plasmonic Metal and Semiconductor Nanoparticle Decorated TiO2-Based Photocatalysts for Solar Light Driven Photocatalysis, in: K. Wandelt (Ed.), Encycl. Interfacial Chem., Elsevier, Oxford, 2018: pp. 786–794. doi:10.1016/B978-0-12-409547-2.13176-2.

[10] S. Ghosh, N.A. Kouamé, L. Ramos, S. Remita, A. Dazzi, A. Deniset-Besseau, P. Beaunier, F. Goubard, P.-H. Aubert, H. Remita, Conducting polymer nanostructures for photocatalysis under visible light, Nat. Mater. 14 (2015) 505–511, https://doi.org/10.1038/nmat4220.

[11] A.D. Becke, Density-functional thermochemistry. III. The role of exact exchange, J. Chem. Phys. 98 (1993) 5648–5652, https://doi.org/10.1063/1.464913.

[12] W. Kohn, L.J. Sham, Self-Consistent Equations Including Exchange and Correlation Effects, Phys. Rev. 140 (1965) A1133–A1138. doi:10.1103/PhysRev.140.A1133.

[13] C. Lee, W. Yang, R.G. Parr, Development of the Colle-Salvetti correlation-energy formula into a functional of the electron density, Phys. Rev. B. 37 (1988) 785–789, https://doi.org/10.1103/PhysRevB.37.785.

[14] B. Miehlich, A. Savin, H. Stoll, H. Preuss, Results obtained with the correlation energy density functionals of becke and Lee, Yang and Parr, Chem. Phys. Lett. 157 (1989) 200–206, https://doi.org/10.1016/0009-2614(89)87234-3.

[15] H. AlRabiah, S. Muthu, F. Al-Omary, A.-M. Al-Tamimi, M. Raja, R.R. Muhamed, A.-A.-R. El-Emam, Molecular structure, vibrational spectra, NBO, Fukui function, HOMO-LUMO analysis and molecular docking study of 6-[(2-methylphenyl) sulfanyl]-5-propylpyrimidine-2,4(1H,3H)-dione, Maced. J. Chem. Chem. Eng. 36 (2017), https://doi.org/10.20450/mjcce.2017.1001.

[16] K.-L. Chen, Y.-W. Yeh, J.-M. Chen, Y.-J. Hong, T.-L. Huang, Z.-Y. Deng, C.-H. Wu, S.-H. Liao, L.-M. Wang, Influence of magnetoplasmonic γ-Fe 2 O 3 /Au core/shell nanoparticles on low-field nuclear magnetic resonance, Sci. Rep. 6 (2016) 35477, https://doi.org/10.1038/srep35477.

[17] C.A. Schneider, W.S. Rasband, K.W. Eliceiri, NIH Image to ImageJ: 25 years of image analysis, Nat. Methods. 9 (2012) 671–675, https://doi.org/10.1038/nmeth.2089.

[18] S.M. Londoño-Restrepo, R. Jeronimo-Cruz, B.M. Millán-Malo, E.M. Rivera-Muñoz, M.E. Rodriguez-García, Effect of the Nano Crystal Size on the X-ray Diffraction Patterns of Biogenic Hydroxyapatite from Human, Bovine, and Porcine Bones, Sci. Rep. 9 (2019), https://doi.org/10.1038/s41598-019-42269-9.

[19] C.F. Holder, R.E. Schaak, Tutorial on Powder X-ray Diffraction for Characterizing Nanoscale Materials, ACS Nano. 13 (2019) 7359–7365, https://doi.org/10.1021/acsnano.9b05157.

[20] J.A. Ramos Guivar, E.A. Sanches, F. Bruns, E. Sadrollahi, M.A. Morales, E.O. López, F.J. Litterst, Vacancy ordered γ-Fe2O3 nanoparticles functionalized with nanohydroxyapatite: XRD, FTIR, TEM, XPS and Mössbauer studies, Appl. Surf. Sci. 389 (2016) 721–734, https://doi.org/10.1016/j.apsusc.2016.07.157.

[21] Chou, Loiland, Lobo, Reverse Water-Gas Shift Iron Catalyst Derived from Magnetite, Catalysts. 9 (2019) 773. doi:10.3390/catal9090773.

[22] A. Ashok, S.N. Vijayaraghavan, S.V. Nair, M. Shanmugam, Molybdenum trioxide thin film recombination barrier layers for dye sensitized solar cells, RSC Adv. 7 (2017) 48853–48860, https://doi.org/10.1039/C7RA08988K.

[23] N.P. Kondekar, M.G. Boebinger, E.V. Woods, M.T. McDowell, In Situ XPS Investigation of Transformations at Crystallographically Oriented MoS 2 Interfaces, ACS Appl. Mater. Interfaces. 9 (2017) 32394–32404, https://doi.org/10.1021/acsami.7b10230.

[24] J. Kaur, M. Singh, C. Dell'Aversana, R. Benedetti, P. Giardina, M. Rossi, M. Valadan, A. Vergara, A. Cutarelli, A.M.I. Montone, L. Altucci, F. Corrado, A. Nebbioso, C. Altucci, Biological interactions of biocompatible and water-dispersed MoS2 nanosheets with bacteria and human cells, Sci. Rep. 8 (1) (2018), https://doi.org/10.1038/s41598-018-34679-y.

[25] L. Chacko, P.K. Rastogi, P.M. Aneesh, Phase Engineering from 2H to 1T-MoS2 for Efficient Ammonia PL Sensor and Electrocatalyst for Hydrogen Evolution Reaction, J. Electrochem. Soc. 166 (2019) H263. doi:10.1149/2.0071908jes.

[26] G. Pagona, C. Bittencourt, R. Arenal, N. Tagmatarchis, Exfoliated semiconducting pure 2H-MoS2 and 2H-WS2 assisted by chlorosulfonic acid, Chem. Commun. 51 (2015) 12950–12953, https://doi.org/10.1039/C5CC04689K.

[27] M.R. Saber, G. Khabiri, A.A. Maarouf, M. Ulbricht, A.S.G. Khalil, A comparative study on the photocatalytic degradation of organic dyes using hybridized 1T/2H, 1T/3R and 2H MoS 2 nano-sheets, RSC Adv. 8 (2018) 26364–26370, https://doi.org/10.1039/C8RA05387A.

[28] R. Ahmad, R. Srivastava, S. Yadav, D. Singh, G. Gupta, S. Chand, S. Sapra, Functionalized Molybdenum Disulfide Nanosheets for 0D–2D Hybrid Nanostructures: Photoinduced Charge Transfer and Enhanced Photoresponse, J. Phys. Chem. Lett. 8 (2017) 1729–1738, https://doi.org/10.1021/acs.jpclett.7b00243.

[29] G. Jia, Y. Zhang, P. Wang, Nano-photo-thermal energy drive MoS_2/ZnO nanoheterojunctions growing, Opt. Mater. Express. 6 (2016) 876, https://doi.org/10.1364/OME.6.000876.

[30] C.-W. Lin, J.-M. Chen, Y.-J. Lin, L.-W. Chao, S.-Y. Wei, C.-H. Wu, C.-C. Jeng, L.-M. Wang, K.-L. Chen, Magneto-Optical Characteristics of Streptavidin-Coated Fe 3 O 4 @Au Core-Shell Nanoparticles for Potential Applications on Biomedical Assays, Sci. Rep. 9 (2019) 16466, https://doi.org/10.1038/s41598-019-52773-7.

[31] K.-L. Chen, Y.-W. Yeh, S.-H. Liao, C.-H. Wu, L.-M. Wang, Study of γ-Fe2O3/Au core/shell nanoparticles as the contrast agent for high-Tc SQUID-based low field nuclear magnetic resonance, in: IEEE 16th Int Conf. Nanotechnol. IEEE-NANO, 2016, pp. 585–586, https://doi.org/10.1109/NANO.2016.7751445.

[32] H. Lu, X. Meng, Correlation between band gap, dielectric constant, Young's modulus and melting point of GaN nanocrystals and their size and shape dependences, Sci. Rep. 5 (2015) 16939, https://doi.org/10.1038/srep16939.

[33] C. Katan, N. Mercier, J. Even, Quantum and Dielectric Confinement Effects in Lower-Dimensional Hybrid Perovskite Semiconductors, Chem. Rev. 119 (2019) 3140–3192, https://doi.org/10.1021/acs.chemrev.8b00417.

[34] B. Ji, E. Rabani, A.L. Efros, R. Vaxenburg, O. Ashkenazi, D. Azulay, U. Banin, O. Millo, Dielectric Confinement and Excitonic Effects in Two-Dimensional Nanoplatelets, ACS Nano. 14 (2020) 8257–8265, https://doi.org/10.1021/acsnano.0c01950.

[35] Z. Xia, H. Fang, X. Zhang, M.S. Molokeev, R. Gautier, Q. Yan, S.-H. Wei, K.R. Poeppelmeier, CsCu 5 Se 3: A Copper-Rich Ternary Chalcogenide Semiconductor with Nearly Direct Band Gap for Photovoltaic Application, Chem. Mater. 30 (2018) 1121–1126, https://doi.org/10.1021/acs.chemmater.7b05104.

[36] A. Jalil, S.Z. Ilyas, S. Ahmed, A. Hassan, D. Li, K. Musselman, Q. Khan, A new 2D Si3X(X=S, 0) direct band gap semiconductor with anisotropic carrier mobility, Surf. Sci. 704 (2021), 121736, https://doi.org/10.1016/j.susc.2020.121736.

[37] W.-G. Lee, S. Chae, Y.K. Chung, W.-S. Yoon, J.-Y. Choi, J. Huh, Indirect-To-Direct Band Gap Transition of One-Dimensional V 2 Se 9: Theoretical Study with Dispersion Energy Correction, ACS Omega. 4 (2019) 18392–18397, https://doi.org/10.1021/acsomega.9b02655.

[38] M. Mahdavi, S. Kimiagar, F. Abrinaei, Preparation of Few-Layered Wide Bandgap MoS2 with Nanometer Lateral Dimensions by Applying Laser Irradiation, Crystals. 10 (2020) 164, https://doi.org/10.3390/cryst10030164.

[39] M. Placidi, Multiwavelength excitation Raman scattering analysis of bulk and two-dimensional MoS2: vibrational properties of atomically thin MoS2 layers, (2015) 11.

[40] M. Ye, D. Winslow, D. Zhang, R. Pandey, Y. Yap, Recent Advancement on the Optical Properties of Two-Dimensional Molybdenum Disulfide (MoS2) Thin Films, Photonics. 2 (2015) 288–307, https://doi.org/10.3390/photonics2010288.

[41] P. Kumar, H. No-Lee, R. Kumar, Synthesis of phase pure iron oxide polymorphs thin films and their enhanced magnetic properties, J. Mater. Sci. Mater. Electron. 25 (2014) 4553–4561, https://doi.org/10.1007/s10854-014-2203-9.

[42] X. Li, J. Li, K. Wang, X. Wang, S. Wang, X. Chu, M. Xu, X. Fang, Z. Wei, Y. Zhai, B. o. Zou, Pressure and temperature-dependent Raman spectra of MoS2 film, Appl. Phys. Lett. 109 (24) (2016) 242101, https://doi.org/10.1063/1.4968534.

[43] F. Li, T.-D. Huang, Y.-W. Lan, T.-H. Lu, T. Shen, K.B. Simbulan, J. Qi, Anomalous lattice vibrations of CVD-grown monolayer MoS2 probed using linear polarized excitation light, Nanoscale. 11 (2019) 13725–13730, https://doi.org/10.1039/C9NR03203G.

[44] P.T. Jochym, J. Łażewski, W. Szuszkiewicz, Phonon mode potential and its contribution to anharmonism, Sci. Rep. 10 (2020) 19783, https://doi.org/10.1038/s41598-020-76454-y.

[45] É. Blanco, P. Afanasiev, G. Berhault, D. Uzio, S. Loridant, Resonance Raman spectroscopy as a probe of the crystallite size of MoS2 nanoparticles, Comptes Rendus Chim. 19 (2016) 1310–1314, https://doi.org/10.1016/j.crci.2015.08.014.

[46] H.-J. Kim, D. Kim, S. Jung, M.-H. Bae, Y.J. Yun, S.N. Yi, J.-S. Yu, J.-H. Kim, D. H. Ha, Changes in the Raman spectra of monolayer MoS2 upon thermal annealing, J. Raman Spectrosc. 49 (2018) 1938–1944, https://doi.org/10.1002/jrs.5476.

[47] A.K. Mishra, K.V. Lakshmi, L. Huang, Eco-friendly synthesis of metal dichalcogenides nanosheets and their environmental remediation potential driven by visible light, Sci. Rep. 5 (2015) 15718, https://doi.org/10.1038/srep15718.

[48] S. Das, G. Swain, K. Parida, One step towards the 1T/2H-MoS2 mixed phase: a journey from synthesis to application, Mater. Chem. Front. 5 (2021) 2143–2172, https://doi.org/10.1039/D0QM00802H.

[49] J. Zhang, Y.-Y. Ma, L.-P. Chen, W.-H. Chen, Experimental and numerical simulation to identify the thermal hazards and hazardous scenarios of N-Nitrodihydroxyethyl dinitrate, Process Saf. Environ. Prot. 145 (2021) 211–221, https://doi.org/10.1016/j.psep.2020.07.040.

[50] D. Mu, Z. Chen, H. Shi, N. Tan, Construction of flower-like MoS2/Fe3O4/rGO composite with enhanced photo-Fenton like catalyst performance, RSC Adv. 8 (2018) 36625–36631, https://doi.org/10.1039/C8RA06537C.

[51] K. Badvi, V. Javanbakht, Enhanced photocatalytic degradation of dye contaminants with TiO2 immobilized on ZSM-5 zeolite modified with nickel nanoparticles, J. Clean. Prod. 280 (2021), 124518, https://doi.org/10.1016/j.jclepro.2020.124518.

[52] L. Acharya, S.P. Pattnaik, A. Behera, R. Acharya, K. Parida, Exfoliated Boron Nitride (e-BN) Tailored Exfoliated Graphitic Carbon Nitride (e-CN): An Improved Visible Light Mediated Photocatalytic Approach towards TCH Degradation and H$_2$ Evolution, Inorg. Chem. 60 (2021) 5021–5033, https://doi.org/10.1021/acs.inorgchem.1c00062.

[53] R.K. Mandal, P. Saha, T.P. Majumder, Structural, optical characterization of the synthesized Fe doped CdO Nano particles, its application as a promising photocatalyst for degradation of the hazardous Methyl violet dye, Optik. 246 (2021), 167795, https://doi.org/10.1016/j.ijleo.2021.167795.

[54] Q. Li, B. Hu, Q. Yang, X. Cai, M. Nie, Y. Jin, L. Zhou, Y. Xu, Q. Pan, L. Fang, Interaction mechanism between multi-layered MoS2 and H2O2 for self-generation of reactive oxygen species, Environ. Res. 191 (2020) 110227, https://doi.org/10.1016/j.envres.2020.110227.

[55] R. Lei, H. Ni, R. Chen, B. Zhang, W. Zhan, Y. Li, Hydrothermal synthesis of WO3/Fe2O3 nanosheet arrays on iron foil for photocatalytic degradation of methylene blue, J. Mater. Sci. Mater. Electron. 28 (2017) 10481–10487, https://doi.org/10.1007/s10854-017-6821-x.

[56] J. Xu, T. Zhang, J. Zhang, Photocatalytic degradation of methylene blue with spent FCC catalyst loaded with ferric oxide and titanium dioxide, Sci. Rep. 10 (2020) 12730, https://doi.org/10.1038/s41598-020-69643-2.

[57] X. Liu, Y. Yang, X. Shi, K. Li, Fast photocatalytic degradation of methylene blue dye using a low-power diode laser, J. Hazard. Mater. 283 (2015) 267–275, https://doi.org/10.1016/j.jhazmat.2014.09.031.

[58] K. Duan, T. Que, S. Koppala, R. Balan, B. Lokesh, R. Pillai, S. David, P. Karthikeyan, S. Ramamoorthy, I.C. Lekshmi, P. Kemacheevakul, N. Padmavathy, S. Munusamy, A facile route to synthesize n-SnO 2 /p-CuFe 2 O 4 to rapidly degrade toxic methylene blue dye under natural sunlight, RSC Adv. 12 (2022) 16544–16553, https://doi.org/10.1039/D2RA01690G.

[59] W. Xu, Y. Jin, Y. Ren, J. Li, Z. Wei, C. Ban, H. Cai, M. Chen, Synergy mechanism for TiO2/activated carbon composite material: Photocatalytic degradation of methylene blue solution, Can. J. Chem. Eng. 100 (2022) 276–290, https://doi.org/10.1002/cjce.24097.

[60] W. Zhang, M. Gao, H. Zhu, Y. Hui, Q. Cao, C. Zhai, Z. Zhang, Microwave-Driven Construction of MoS2/Graphene Heterostructure for Enhanced Photodegradation under Natural Light, Phys. Status Solidi A. 219 (2022) 2100767, https://doi.org/10.1002/pssa.202100767.

[61] M. Xie, X. Liu, S. Wang, Degradation of methylene blue through Fenton-like reaction catalyzed by MoS2-doped sodium alginate/Fe hydrogel, Colloids Surf. B Biointerfaces. 214 (2022) 112443, https://doi.org/10.1016/j.colsurfb.2022.112443.

[62] J. Niu, Y. Zhang, J. Shi, Z. Zhang, Z. Ma, B. Yao, X. Yu, X. Wang, Microwave-based preparation of γ-Fe2O3/SrTiO3 photocatalyst for efficient degradation of organic pollutants in water, Mater. Chem. Phys. 288 (2022) 126357, https://doi.org/10.1016/j.matchemphys.2022.126357.

[63] S. Hmamouchi, A. El Yacoubi, B.C. El Idrissi, Using egg ovalbumin to synthesize pure α-Fe2O3 and cobalt doped α-Fe2O3: structural, morphological, optical and photocatalytic properties, Heliyon. 8 (2) (2022) e08953, https://doi.org/10.1016/j.heliyon.2022.e08953.

[64] A.P. Bhat, P.R. Gogate, Degradation of nitrogen-containing hazardous compounds using advanced oxidation processes: A review on aliphatic and aromatic amines, dyes, and pesticides, J. Hazard. Mater. 403 (2021), 123657, https://doi.org/10.1016/j.jhazmat.2020.123657.

[65] H. Kim, H. Kim, S. Weon, G. Moon, J.-H. Kim, W. Choi, Robust Co-catalytic Performance of Nanodiamonds Loaded on WO3 for the Decomposition of Volatile Organic Compounds under Visible Light, ACS Catal. 6 (2016) 8350–8360, https://doi.org/10.1021/acscatal.6b02726.

[66] Y. Zhang, J. Zhang, B. Zhang, R. Si, B. Han, F. Hong, Y. Niu, L. Sun, L. Li, B. Qiao, K. Sun, J. Huang, M. Haruta, Boosting the catalysis of gold by O2 activation at Au-SiO2 interface, Nat. Commun. 11 (2020) 558, https://doi.org/10.1038/s41467-019-14241-8.

[67] T. Ahmed, S. Balendhran, M.N. Karim, E.L.H. Mayes, M.R. Field, R. Ramanathan, M. Singh, V. Bansal, S. Sriram, M. Bhaskaran, S. Walia, Degradation of black phosphorus is contingent on UV–blue light exposure, Npj 2D Mater. Appl. 1 (2017) 1–7, https://doi.org/10.1038/s41699-017-0023-5.

[68] Y. Li, J.G. DiStefano, A.A. Murthy, J.D. Cain, E.D. Hanson, Q. Li, F.C. Castro, X. Chen, V.P. Dravid, Superior Plasmonic Photodetectors Based on Au@MoS$_2$ Core-Shell Heterostructures, ACS Nano. 11 (2017) 10321–10329, https://doi.org/10.1021/acsnano.7b05071.

[69] S. Tang, M. Zhao, D. Yuan, X. Li, Z. Wang, X. Zhang, T. Jiao, J. Ke, Fe3O4 nanoparticles three-dimensional electro-peroxydisulfate for improving tetracycline degradation, Chemosphere. 268 (2021), 129315, https://doi.org/10.1016/j.chemosphere.2020.129315.

[70] R. Lei, H. Ni, R. Chen, H. Gu, B. Zhang, W. Zhan, Hydrothermal synthesis of CdS nanorods anchored on α-Fe2O3 nanotube arrays with enhanced visible-light-driven photocatalytic properties, J. Colloid Interface Sci. 514 (2018) 496–506.

[71] L. Yang, S. Guo, X. Li, Au nanoparticles@MoS2 core-shell structures with moderate MoS2 coverage for efficient photocatalytic water splitting, J. Alloys Compd. 706 (2017) 82–88, https://doi.org/10.1016/j.jallcom.2017.02.240.

[72] R. Lei, H. Ni, R. Chen, H. Gu, B. Zhang, Novel ZnO nanoparticles modified WO3 nanosheet arrays for enhanced photocatalytic properties under solar light illumination, Appl. Surf. Sci. 463 (2019) 363–373, https://doi.org/10.1016/j.apsusc.2018.08.218.

[73] M. Saranya, S. Ayyappan, R. Nithya, R.K. Sangeetha, A. Gokila, MOLECULAR STRUCTURE, NBO AND HOMO-LUMO ANALYSIS OF QUERCETIN ON SINGLE LAYER GRAPHENE BY DENSITY FUNCTIONAL THEORY, (n.d.) 9.

[74] D. Lungerich, O. Papaianina, M. Feofanov, J. Liu, M. Devarajulu, S.I. Troyanov, S. Maier, K. Amsharov, Dehydrative π-extension to nanographenes with zig-zag edges, Nat. Commun. 9 (2018) 4756, https://doi.org/10.1038/s41467-018-07095-z.

[75] S. Mohd, M.A. Ali, H.A. Farah, K.-A. Al-Lohedan, Comprehensive exploration of the anticancer activities of procaine and its binding with calf thymus DNA: a multi spectroscopic and molecular modelling study, RSC Adv. 8 (2018) 9083–9093, https://doi.org/10.1039/C7RA13647A.

[76] R. Srivastava, L.R. Joshi, The effect of substituted 1,2,4-triazole moiety on the emission, phosphorescent properties of the blue emitting heteroleptic iridium(III) complexes and the OLED performance: a theoretical study, Phys Chem Chem Phys. 16 (2014) 17284–17294, https://doi.org/10.1039/C4CP02368D.

[77] G.E.S.M. J. Frisch, G. W. Trucks, H. B. Schlegel, B.M.M. A. Robb, J. R. Cheeseman, G. Scalmani, V. Barone, H.P.H.G. A. Petersson, H. Nakatsuji, M. Caricato, X. Li, M. H.A. F. Izmaylov, J. Bloino, G. Zheng, J. L. Sonnenberg, T.N.M. Ehara, K. Toyota, R. Fukuda, J. Hasegawa, M. Ishida, J.Y. Honda, O. Kitao, H. Nakai, T. Vreven, J. A. Montgomery, E.B.J. E. Peralta, F. Ogliaro, M. Bearpark, J. J. Heyd, J.N.K. N. Kudin, V. N. Staroverov, R. Kobayashi, J.T.K. Raghavachari, A. Rendell, J. C. Burant, S. S. Iyengar, J.B.C.M. Cossi, N. Rega, J. M. Millam, M. Klene, J. E. Knox, R.E.S.V. Bakken, C. Adamo, J. Jaramillo, R. Gomperts, J.W.O.O. Yazyev, A. J. Austin, R. Cammi, C. Pomelli, G.A.V.R. L. Martin, K. Morokuma, V. G. Zakrzewski, A.D.D.P. Salvador, J. J. Dannenberg, S. Dapprich, J.C.O. Farkas, J. B. Foresman, J. V. Ortiz, and D.J.Fox, Gaussian 09, Revision A.02, (2009).